Fibers and Polymers 2022, Vol.23, No.10, 2732-2739
DOI 10.1007/s12221-022-0043-4

ISSN 1229-9197 (print version)
ISSN 1875-0052 (electronic version)

Investigation on the Airflow Fields of New Melt-blown Dies with Rectangular Jets

Yudong Wang[1], Fang Jiang[1], Wan'e Ning[1], Sheng Xie[2,3]*, and Changchun Ji[1,4]*

[1]*College of Biological and Chemical Engineering, Guangxi University of Science and Technology, Liuzhou 545006, China*
[2]*Key Laboratory of Yarn Materials Forming and Composite Processing Technology of Zhejiang Province, Jiaxing University, Jiaxing 314001, China*
[3]*Nanotechnology Research Institute, Jiaxing University, Jiaxing 314001, China*
[4]*Shanxi Institute of Energy, Jinzhong 030600, China*

(Received January 17, 2022; Revised March 21, 2022; Accepted March 25, 2022)

Abstract: In order to reduce the fiber diameter and the energy consumption in the melt-blowing process, three new slot dies (slot die with air accelerator, slot die with stabilizers and slot die with extensions) are designed. The airflow fields of these dies have been numerically calculated and experimentally verified. The results reveal that the slot die with stabilizers and slot die with extensions have higher average stagnation temperatures, average air pressure and average turbulent kinetic energy than those of the common slot die. Compared with the common slot die, the slot die with air accelerator could increase the average stagnation temperature on the spinning line, however, its average pressure is reduced and the average turbulent kinetic energy is locally increased. By comprehensively comparing the average stagnation temperature, average air pressure and average turbulent kinetic energy on the spinning lines of these slot dies, the new slot die with stabilizers is the most conducive to the attenuation of the melt-blowing fibers and the reduction of energy consumption. The research in this work can have strong guiding significance for the optimization of die structure and the attenuation of melt-blowing fibers.

Keywords: Melt blowing, Airflow field, New die, Numeral calculations, Fiber attenuation

Introduction

Due to the properties of small diameter and large specific surface area, ultra-fine fibers have excellent characteristics, such as good water absorption, oil removal, warmth retention and gloss that greatly expands the application fields and development prospects of textile fibers. Therefore, the equipment and technology for producing ultra-fine fibers have also become research hotspots [1-4]. Currently, as one of the most popular methods for producing ultra-fine fibers, melt blowing is a mature technology with advantages of high production efficiency and large output. The diameter of melt-blown fiber can be as small as several hundred nanometers, and it is usually distributed between 1-4 microns [5,6]. Melt-blown materials are used as medical materials, sound insulation materials, heat preservation materials, filter materials, battery separators and dust-free wipes, etc [7,8].

As shown in Figure 1, melt blowing is the utilization of high-temperature airflow generated by the die head to rapidly stretch the polymer melt extruded from the spinneret to form micron-sized fibers. The airflow field below the melt-blown die not only affects the fineness of the fiber, but also determines the fiber diameter evenness. Therefore, a lot of research work related to the spinning die and the underneath air flow field have been launched. Harpham and Shambaugh [9,10] experimental studied the speed distribution of a slot-die melt blowing with a large length-to-width ratio at room temperature. They also measured the distribution of the flow field formed in the slot die above under non-isothermal conditions by using mainly used pitot tubes and thermocouples as measuring tools, and obtained the empirical formula of air velocity on the spinning line. Tate and Shambaugh [11] used similar experimental methods to study the air velocity distribution in the flow field below the sharp die. Chen [12] and Wang [13] utilized hot wire anemometer and laser doppler anemometer to collect data on air flow field under the melt-blown die, and discovered some new rules of the airflow field. The structure and size of the slot die have a great influence on the airflow velocity and airflow temperature. Xie *et al*. [14-16] used a hot wire

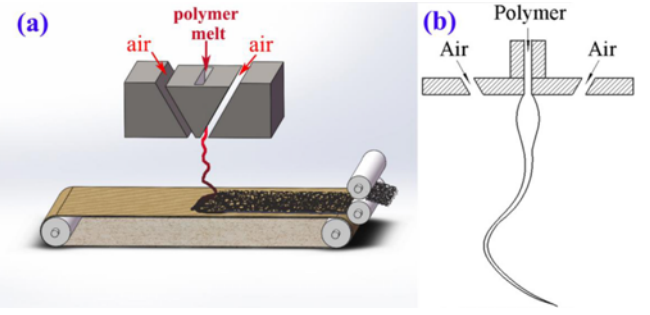

Figure 1. (a) Schematic process of the slot-die melt blowing and (b) structure relationship between the airslot and the polymeric fiber.

*Corresponding author: xie@zjxu.edu.cn
*Corresponding author: chuangchun_ji@163.com

anemometer and a high-speed camera to investigate the relationship between the air velocity fluctuation and the fiber whipping in the slot-die melt blowing. Yang and Zeng [17] collected the velocity distribution data of the turbulence field under the common slot die using a hot wire anemometer with a two-dimensional probe. Wang *et al*. [18,19] measured three-dimensional flow field under the slot die.

Because Pitot tubes, hot wire anemometers, and thermocouples are all contact measurement tools, they would have an unavoidable impact on the airflow field, which makes the measured data and the true value have a certain error. With the popularization of computers, many current researchers tend to use computational fluid dynamics (CFD) to simulate the flow field under the melt-blown die. CFD can obtain the airflow field velocity, temperature distribution, turbulence intensity distribution and fluid density distribution in the area close to the melt-blown die, which is difficult to measure with instruments.

In the year of 2002, Krutka *et al*. [20] used CFD to conduct a numerical study on the air flow field under the slot die, and obtained air velocity cloud and vector diagrams. In the numerical simulation, three turbulence models were tested with inlet velocity lower than 34.6 m/s. In addition, in order to calculate more accurately, they revised the parameters of the turbulence model. A few years later, they [21,22] used CFD approach investigate the influence of the structure of the melt-blown die on the flow field distribution. The results revealed that when the air-slot inclination of the die head decreases, the air velocity and turbulence pulsation also increase. Sun and Wang [23,24] proposed stagnation temperature as an objective function to optimize the design of melt-blown die, they performed numerical calculations on a series of slot dies and got the best structure of common die. Hao *et al*. [25] performed numerical calculations on the coupled flow field of air and fibers under the slot die, and studied the effect of process parameters on the jet flow. Wang *et al*. [26-28] designed a series of new slot dies and investigated the influence of their structure on the speed of the spinning line in the flow field by means of numerical calculations.

Figure 2a shows a common slot die, which is also called a blunt die and commonly used in lots of previous work. However, the gas heat transfer and turbulence characteristics analysis indicated that the jet of the common slot die has a certain amount of kinetic energy loss and heat dissipation during the fiber attenuation process. Moreover, there is a triangular recirculation zone under the nose of the common slot die, which is filled with separation vortices and causes kinetic energy loss [29]. In order to reduce the kinetic energy loss and thermal energy loss of the drafting airflow and obtain finer melt-blown fibers, we designed several new die heads and performed numerical analysis on their flow fields.

Experimental

Structure of the Slot Die

The structure of the melt-blown die head determines the distribution of velocity, temperature, turbulence intensity and pressure of the air flow field [11-13,21,22]. Therefore, redesigning the die head is expected to achieve the purpose of optimizing air flow field. In the present work, three new dies are designed on the basis of the common slot die (denoted as Die 1, as shown in Figure 2). Die 1 and the following three new slot dies have several same structural parameters, including the air slot width e=0.65 mm, the inclination angle α=60 ° of air slot relative to the plate, and the nose width f=1.28 mm respectively.

As shown in Figure 2b, Die 2 has an air-velocity increaser on the plates of the both sides. The design purpose of the two air-velocity increasers is to reduce the spread of the fused jets to both sides, and to increase the speed and temperature of the drafting airflow on the center line of the flow field. The two air-velocity increasers are exactly the same size, and their shape is rectangular parallelepiped. The distance b from the bottom surface of the two air-velocity increasers to the plate is 20 mm. The distance h from the spinneret axis to

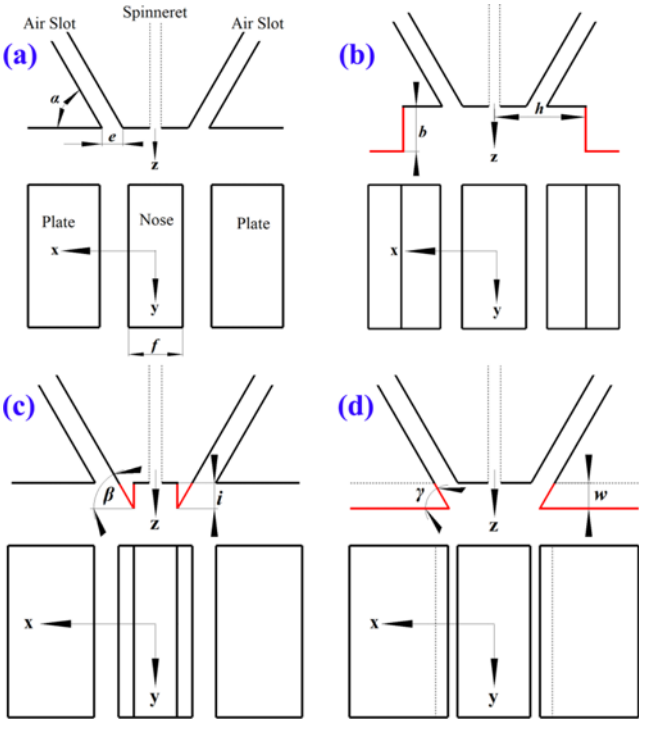

Figure 2. Structure of the melt-blown die; (a) structure of common slot die (Die 1), (b) structure of Die 2, it has an air-velocity increaser on the plates of the both sides, (c) structure of Die 3, it has two stabilizer pieces on the two outside of its nose, and (b) structure of Die 4, it has an extension on the outside of the air slot.

the two sides of the two air-velocity increasers, which are parallel to the z-axis, is 10 mm. Figure 2c shows the structure of Die 3, which has two stabilizer pieces on the two outside of its nose. The stabilizer piece aims to reduce the internal diffusion of two independent jets. The cross section of the stabilizer piece is a right triangle. Its slope is an extension of the wall of the air slot near the nose, and the inclination angle β is 60 °. The height i of the stabilizer piece, which is the distance from the tip to the nose, is 0.8 mm. As shown in Figure 2d, Die 4 has an extension on the outside of the air slot. The distance w between the bottom of the extension and the nose is 0.8 mm, which is the same as the height i of the die 3. The angle γ between the bottom of the extension and the air slot is 60 °. The extension function is to prevent two independent jets from spreading outward and reduce the loss of the kinetic energy and the heat energy.

As shown in Figure 2, the origin of coordinate systems is located at the center point of the spinneret outlet. The z-axis is perpendicular to the lateral die face, and its positive direction is consistent with the movement direction of the melt-blown fiber. The x-axis is parallel to the lateral die face. The y-axis is parallel to the air slots and perpendicular to the centerline (i.e., z-axis) of the spinneret.

Computational Domain

Due to the three-dimensional air flow field under the slot die has two-dimensional characteristics [9,30]. Therefore, in the present work, we take a two-dimensional calculation of the flow fields under the common die head and the remaining three new slot dies. In order to facilitate the calculation of the two-dimensional flow field, it is assumed that the length of the air accelerator, the stabilizer, and the plate extension along the y-axis direction is equal to that of the air slot and meets the calculation requirements. The two-dimensional airflow field of the slot die is axisymmetric, Figure 3 shows half of the area needs to be calculated numerically for the common Die 1. The computational domain includes two parts of the air slot and the flow field under the nose, and its coordinate system is the same as that in Figure 2. The length of the air slot along the z-axis is 5 mm. The size of the remaining space part along the x-axis direction and that along the z-axis direction are 30 mm and 100 mm, respectively. The two-dimensional computational domain of Die 2, Die 3, and Die 4 are similar to that of Die 1, but they are not be shown in this work.

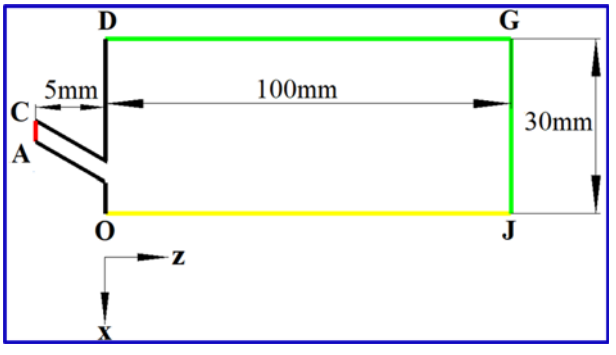

Figure 3. Computational domain of two-dimensional flow field for Die 1.

Grid Size

In the Gambit software, the initial grid size is 0.1 mm. Then, in the computational domain, we use Fluent software to further reduce the mesh size in the local area to 0.05 mm. The area with a smaller mesh size is within a range of 30 mm below the origin along the fiber stretching direction and 6 mm perpendicular to the fiber movement direction. The division method refers to the previous research [20], which ensure that the calculated data has a high calculation accuracy and is not affected by the number of grids.

Turbulence Model

The shear stress transport model (SST model) was used in this simulation, the SST model [31] is a two-equation model, which could not only capture the flow in the core area of turbulence like the standard k-ε model, but also has a wide range of application and accuracy in the free flow near the wall like the standard k-ω model. In the flow field below the slot die, there is both a turbulent core area and a near-wall flow area. Therefore, in theory, the effect of applying the SST model should be very good.

The two equations contained in the SST model are as follows:

$$\frac{\partial}{\partial t}(\rho k)+\frac{\partial}{\partial x_i}(\rho u_i k)=\tilde{G}_k-\beta^*\rho k\omega+\frac{\partial}{\partial x_i}\left[(\mu+\sigma_k\mu_t)\frac{\partial k}{\partial x_i}\right] \quad (1)$$

$$\frac{\partial(\rho\omega)}{\partial t}+\frac{\partial(\rho u_i\omega)}{\partial x_i}=\alpha\rho S^2-\beta\rho\omega^2+\frac{\partial}{\partial x_i}\left[(\mu+\sigma_\omega\mu_t)\frac{\partial\omega}{\partial x_i}\right]$$
$$+2(1-F_1)\rho\sigma_{\omega 2}\frac{1}{\omega}\frac{\partial k}{\partial x_i}\frac{\partial\omega}{\partial x_i} \quad (2)$$

In equations (1) and (2), μ_t is the turbulent viscosity, which could be expressed by the following equation (3).

$$\mu_t=\frac{\rho k}{\omega}\frac{1}{\max\left[\frac{1}{\alpha^*},\frac{SF_2}{a_1\omega}\right]} \quad (3)$$

F_1 and F_2 are two empirical mixed functions, which could be expressed by equation (4) and equation (5).

$$F_1=\tanh\left\{\left\{\min\left[\max\left(\frac{\sqrt{k}}{\beta^*\omega Y},\frac{500\mu}{\rho Y^2\omega}\right),\frac{4\rho\sigma_{\omega 2}k}{CD_{k\omega}Y^2}\right]\right\}^4\right\} \quad (4)$$

$$F_2=\tanh\left[\left[\max\left(\frac{2\sqrt{k}}{\beta^*\omega Y},\frac{500\mu}{\rho Y^2\omega}\right)\right]^2\right] \quad (5)$$

The auxiliary relations are as follows.

$$\tilde{G}_k = \min\left(G_k, 10\beta^* \rho k\omega\right) \tag{6}$$

$$G_k = \mu_t \frac{\partial u_i}{\partial x_j}\left(\frac{\partial u_i}{\partial x_j} + \frac{\partial u_j}{\partial x_i}\right) \tag{7}$$

$$CD_{k\omega} = \max\left(2\rho\sigma_{\omega 2}\frac{1}{\omega}\frac{\partial k}{\partial x_i}\frac{\partial \omega}{\partial x_i},\ 10^{-10}\right) \tag{8}$$

Y is the distance to the nearest wall. Some factors are assigned the following values.

β^*=0.09, α_1=5/9, β_1=3/40, σ_{k1}=0.85, $\sigma_{\omega 1}$=0.5, α_2=0.44, β_2=0.0828, σ_{k2}=1.0, $\sigma_{\omega 2}$=0.856, a_1=0.31.

The remaining parameters are detailed in literature [31].

Boundary Conditions

As shown in Figure 3, taking Die 1 for an example, line A-C was the pressure inlet boundary, the air pressure was set to be 1.2 atm, and its temperature was 400 K, its hydraulic diameter was 0.65 mm and 10 % respectively. Line O-J was symmetry boundary. Lines D-G and G-J were pressure outlet, the air pressure and temperature were 1 atm and 300 K, respectively. The turbulence intensity of the backflow was the same as that at boundary A-C, and the length scale was 10 mm. The rest of the line segments are boundary of wall, and the temperatures here were all 480 K.

Experiment Verification

In the previous work [19], we used a hot-wire anemometer to measure the three-dimensional airflow field under the common slot die on-line. For the validity of the numerical calculations in this article, the experimental results measured by the hot wire anemometer and the numerical calculation data obtained by applying the SST model are compared in this section. Figure 4 shows that both CFD data and experimental measurement data gradually increase to a peak and then drop rapidly. It could be found in Figure 4 that the velocity on the center line of the flow field measured by the hot wire anemometer is basically consistent with the simulation result calculated by the SST model.

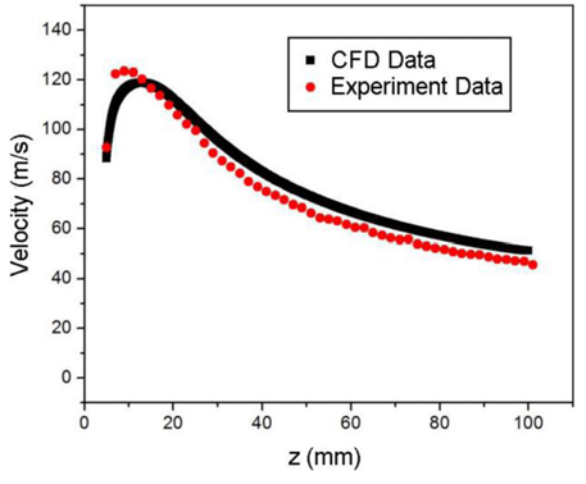

Figure 4. CFD data and experimental data on the z-axis. The pressure of the air at the intake valve is 0.05 MPa and the temperature is 310K.

Results and Discussion

Stagnation Temperature Distribution on the z-axis

In the process of melt-blown process, the air attenuated the polymer melt into fine fibers, and the air force is squared with the relative speed of the fiber and the air stream [32,33]. As a result, increasing the air speed can significantly strong the drafting effect [34,35]. However, just increasing the airflow speed does not necessarily reduce the fineness of the fiber to the greatest extent, because the airflow temperature can also affect the stretching of the fiber. Therefore, if the airflow temperature is higher, the attenuation rate of the polymer temperature could be reduced, resulting in increasing the stretching distance of the fiber, which is beneficial to obtain finer fibers.

The stagnation temperature T^* is a parameter used to describe the stagnation state at a certain point in the airflow field. It is the total internal energy obtained by adding the internal energy converted from the kinetic energy of the airflow and the enthalpy at the stagnation point. Therefore, the stagnation temperature is actually composed of two parts, namely dynamic temperature and static temperature, as shown in equation (9).

$$T^* = T + \frac{v_a^2}{2C_{pa}} \tag{9}$$

In equation (9), T^* is the total temperature of the gas, T is the static temperature of the gas, v_a is the velocity of the gas, C_{pa} is the specific heat capacity of the gas, and $v_a^2/2C_{pa}$ is the dynamic temperature of the gas.

Equation (9) reveals that the total temperature can reflect the combined effect of the velocity and temperature of the gas jet, so it is more suitable to describe the performance of the gas flow field.

In the melt-blown process, the fiber mainly moves in the area near the spinning line (i.e., z-axis), and the main fiber attenuation occurs within 15 mm below the die head [34]. Therefore, we mainly investigate the changes of physical parameters on the z-axis. Figure 5 shows the stagnation temperature curves of four slot dies on the z-axis. It shows that the stagnation temperatures of the three new die melt blowing are higher than that of the common die. It reveals that weakening the diffusion of the jet to the surroundings is beneficial to reducing the kinetic energy loss or thermal energy loss of the airflow, which is beneficial to the refinement of the fiber diameter and energy saving. Die 3

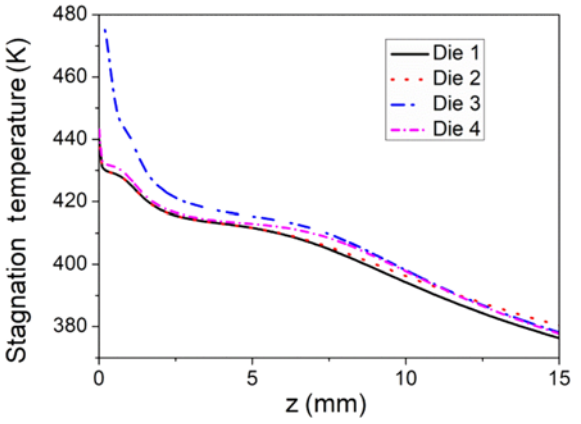

Figure 5. Stagnation temperature distributions on the spinning lines.

has the highest stagnation temperature on the z-axis. The average stagnation temperatures on the center lines of the flow field below Die 1, Die 2, Die 3, and Die 4 are 427.36 K, 428.72 K, 451.23 K, and 429.674 K. When the average stagnation temperature on the spinning line increases, it means that the drafting speed and air temperature around the polymer melt are higher, and the finer melt blowing fibers could be produced. Therefore, using the average stagnation temperatures as the fiber thinning indicators, the structural design of the slot die with the two stabilizers is the most reasonable.

Figure 6 shows the velocity vector diagrams under the four slot dies, respectively. Compared Figure 6a and Figure 6b, the recirculation zones under Die 1 and Die 2 are almost identical. The air accelerator could block the air jet from diffusing outward, and could transfer heat around the spinning thread by means of heat conduction, heat radiation and convection heat transfer. As a result, within the range of 8 mm $\leq z \leq$ 15 mm, it could increase the velocity and temperature on the center line of the flow field below. Figure 6c shows that the stabilizers in Die 3 reduce the area of the triangular recirculation zone and the generation of vortex clusters. However, the extension of Die 4 in Figure 6d has no effect on the recirculation zone under the nose. In addition, the stabilizers and the outer end extension could reduce the inward or outward diffusion of two independent jets, which helps to reduce the dissipation of kinetic energy and thermal energy and increase the stagnation temperature on the z-axis. Through the comparison of the curves in Figure 8, it could be found that the effect of eliminating the inward diffusion of independent jets is better.

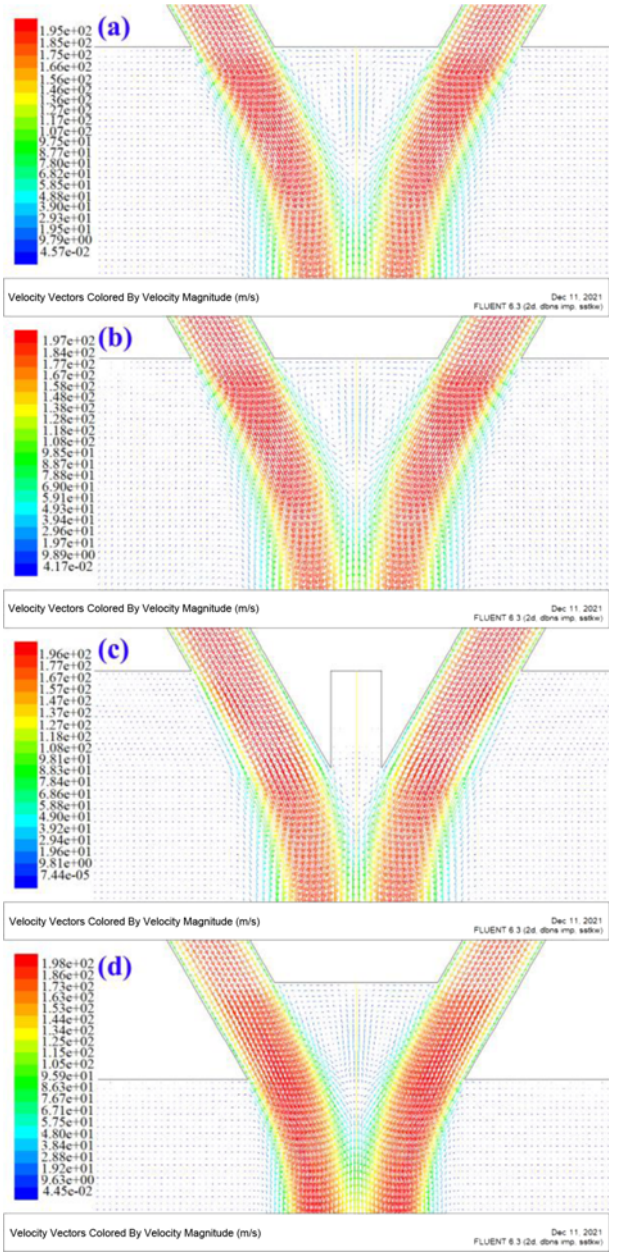

Figure 6. (a) Velocity vector of die 1, (b) velocity vector of die 2, (c) velocity vector of die 3, and (d) velocity vector of die 4.

Pressure Distribution on the z Axis

Figure 7 reveals the distributions of air pressure at the centerlines below the common die (i.e., Die 1) and three new slot dies. The pressure distribution of the slot dies is very similar to that of air velocity. In the beginning, Die 3 has the highest pressure, and Die 4 has the second highest pressure. Among them, only Die 2 has a lower pressure than the common slot die. The peak airflow pressure in the Die 4 flow field is the largest, and the advantage is obvious. The pressure peaks on the centerline of the flow field below Die 3, Die 1, and Die 2 gradually decrease, and the difference between them is small. In the range of 2.5 mm $\leq z \leq$ 15 mm, the pressure values on the spinning lines of Die 1, Die 3 and Die 4 are exactly the same, and they are higher than that of Die 2. The curves in Figure 7 illustrate that the air

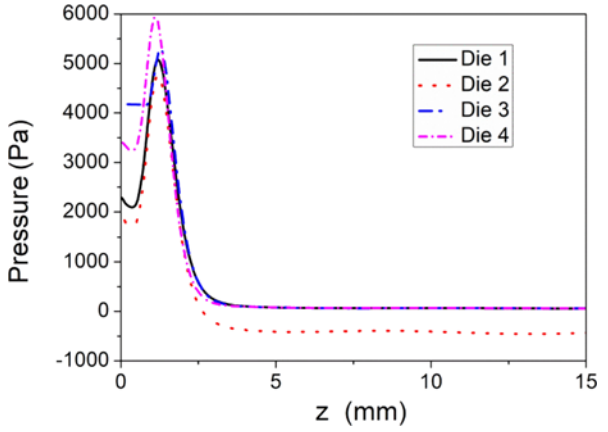

Figure 7. Pressure distributions on the spinning lines.

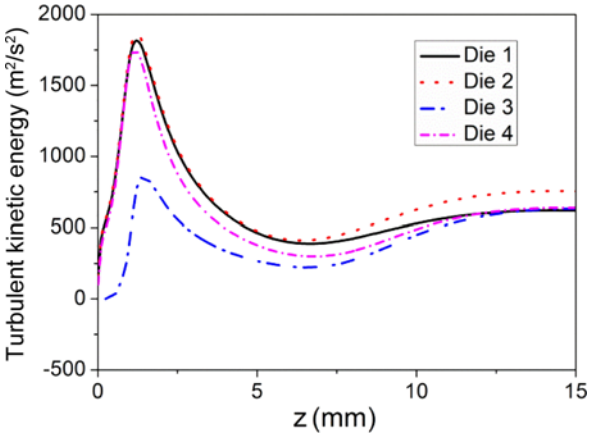

Figure 8. Turbulent kinetic energy distributions on the spinning lines.

accelerator, the stabilizer, and the extension have a certain influence on the pressure distribution in the flow field below the slot die.

When the air pressure value on the center line increases, there would be greater radial pressure around the polymer melt surface, which is more conducive to the drafting of the melt-blown fiber. The air pressure peaks on the spinning lines in the flow fields below Die 1, Die 2, Die 3, and Die 4 are 5079.93 Pa, 4771.73 Pa, 5306.43 Pa, and 5,962.32 Pa, respectively. Taking maximum pressure as a reference indicator, the attenuating effect of Die 1 on fibers is weaker than those of Die 3 and Die 4, and slightly stronger than that the die 2. The average air pressures on the center lines of Die 1, Die 2, Die 3, and Die 4 are 3376.165484 Pa, 3031.500323 Pa, 4452.331935 Pa, and 4275.758182 Pa, respectively. From the perspective of average air pressure, Die 3 is the most conducive to fiber diameter reduction.

Combined with Figure 6a, Figure 6c, and Figure 6d, the stabilizers and the extension reduce the kinetic energy loss of the two independent jets, making the collision of the two jets more intense when they merge. Therefore, compared with Die 1, the peak air pressure on the spinning line of the flow field under Die 4 and Die 3 is larger. Figure 6b shows that the air accelerator could bounce the diffused air flow, but due to the Coanda effect, it has a tendency to attract jets to the side of the accelerator. The result is that the mean pressure of the flow field from Die 2 is the smallest of the four.

Turbulent Kinetic Energy Distribution on the z-axis

Figure 8 reveals the turbulent kinetic energy values on the z-axis below these four slot dies. As shown in Figure 8, the turbulent kinetic energy peaks of the Die 1 and Die 2 are almost the same and slightly higher than that of Die 4. In addition, the maximum value of turbulent kinetic energy on the center line of the flow field from Die 3 is the smallest of the four. In the range of 10 mm$\leq z \leq$15 mm, the turbulent kinetic energy of the spinning line of Die 2 is the highest among all die heads. Furthermore, within this range of 10 mm$\leq z \leq$15 mm, the turbulent kinetic energy curve of the slot die with the extension (Die 4) and the slot die with the stabilizer (Die 3) are lower than that of the common die head. Turbulent kinetic energy is an indicator to measure the development or decline of turbulence. When the turbulent kinetic energy of the airflow increases, its instantaneous velocity difference and fluctuation become larger. Comparing Figure 6a, Figure 6b, Figure 6c and Figure 6d, the triangular recirculation zones in the flow fields of Die 1, Die 2 and Die 4 are basically the same. Therefore, there is almost no difference in the peak values of turbulent kinetic energy on their spinning lines. Because the stabilizers could reduce the number of vortex clusters and make the flow in the area smoother, the maximum value of the turbulent kinetic energy of Die 3 is much smaller than that of Die 1.

The trajectory of the melt blown fiber under the action of the drafting airflow is shown in Figure 9. It was shot with a high-speed camera of the brand RADLAKE, which has a shooting speed of 5000 f/s. It could be seen from Figure 9 that the fibers whips violently. When the turbulent kinetic energy of the drafting air flow is greater, the amplitude of the fiber would increase. It would make the melt-blown fiber stick to the nose or the plates, and even cause the fiber breakage. Therefore, it is generally believed that the smaller the peak value of turbulent kinetic energy, the more conducive to fiber production.

The peak values of turbulent kinetic energy in the airflow fields of Die 1, Die 2, Die 3 and Die 4 are 1814.3 m^2/s^2, 1860.47 m^2/s^2, 861.155 m^2/s^2 and 1755.46 m^2/s^2, respectively. The average values of turbulent kinetic energy on the spinning lines of Die 1, Die 2, Die 3, and Die 4 are 1169.468968 m^2/s^2, 1199.762581 m^2/s^2, 283.6335907 m^2/s^2 and 1065.929442 m^2/s^2, respectively. Taking the maximum and average values of turbulent kinetic energy as a reference

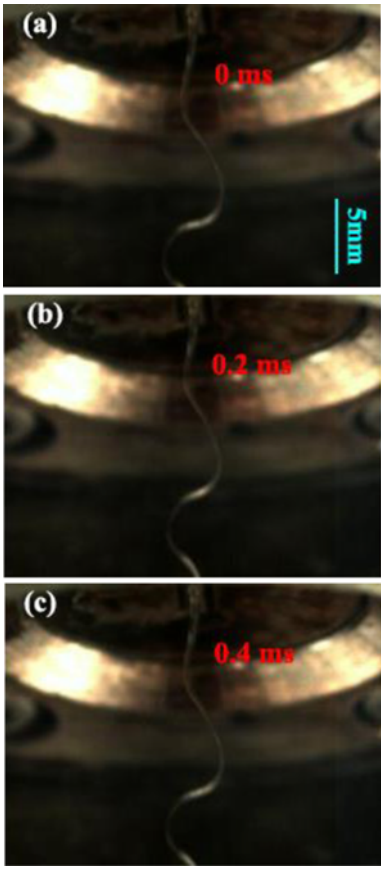

Figure 9. Motion trajectory of melt-blown fiber at time instants of (a) 0 ms, (b) 0.2 ms, and (c) 0.4 ms. Experimental conditions: inlet air pressure of 0.05 MPa, the fiber motion was captured with velocity of 5000 frame/s, the polymer flow rate of 7.8 cc/min.

indicator, among the three new slot dies, compared to Die 1, Die 3 has the best effect, Die 4 is also more conducive to the smooth drafting of fibers, and Die 2 would slightly intensify the degree of fiber whiplash.

Conclusion

In this work, in order to achieve the purpose of refining the melt-blown fiber, we designed several new slot dies, and used Gambit to establish their calculation domain and Fluent to perform numerical calculations on them. The numerical simulation data was compared with the experimental data to verify the validity of the calculation.

Numerical calculation results show that taking stagnation temperature as a measurement index, the slot die with the stabilizers is most helpful for the attenuation of the melt-blown fibers. Using the peak air pressure as an indicator, the slot die with the extension could be more conducive to fiber thinning. However, from the point of view of the average pressure on the spinning line, the die with two stabilizers is the best. Taking the peak value and average value of turbulent kinetic energy as the reference value, the slot die with the two stabilizers is more conducive to the smooth drafting of the melt-blown fiber. Taken together, the new slot die with the stabilizers has the best effect in reducing fiber diameter and production energy consumption among all die heads.

Acknowledgement

This research was supported by the National Natural Science Foundation of China (No. 11702113), the Open Project Program of Key Laboratory of Yarn Materials Forming and Composite Processing Technology of Zhejiang Province (MTC-2022-2), the Doctoral Fund Program of Guangxi University of Science and Technology (21Z47), the Natural Science Foundation of Inner Mongolia (Grant No. 2021LHMS01003) and Fujian Natural Science Foundation Project (Grant No.2019J01740).

Conflict of Interest

The author(s) declared no potential conflicts of interest with respect to the research, author-ship, and/or publication of this article.

References

1. Y. Q. Xu, X. M. Zhang, X. B. Hao, D. F. Teng, T. N. Zhao, and Y. C. Zeng, *Chem. Eng. J.*, **423**, 130175 (2021).
2. D. F. Teng, A. Wahid, and Y. C. Zeng, *Polymer*, **201**, 122609 (2020).
3. W. L. Han, S. Xie, J. Shi, and X. H. Wang, *Polym. Eng. Sci.*, **59**, 1182 (2019).
4. B. W. Zhu, S, Xie, W. L. Han, and G. J. Jiang, *Fiber. Polym.*, **22**, 1594 (2021).
5. W. L. Han, G. S. Bhat, and X. H. Wang, *Ind. Eng. Chem. Res.*, **55**, 3150 (2016).
6. X. B. Hao and Y. C. Zeng, *Ind. Eng. Chem. Res.*, **58**, 11624 (2019).
7. Z. F. Wang, C. W. Macosko, and F. S. Bates, *ACS Appl. Mater. Inter.*, **8**, 3006 (2016).
8. H. Zhang, Q. Zhen, Y. Liu, L. Wang, X. Y. Guan, and Y. F. Zhang, *J. Ind. Text.*, **51**, 1431 (2020).
9. A. S. Harpham and R. L. Shambaugh, *Ind. Eng. Chem. Res.*, **35**, 3776 (1996).
10. A. S. Harpham and R. L. Shambaugh, *Ind. Eng. Chem. Res.*, **36**, 3937 (1997).
11. B. D. Tate and R. L. Shambaugh, *Ind. Eng. Chem. Res.*, **43**, 5405 (2004).
12. T. Chen, X. H. Wang, and X. B. Huang, *Text. Res. J.*, **74**, 1018 (2004).
13. X. M. Wang and Q. F. Ke, *Polym. Eng. Sci.*, **45**, 1092 (2005).

14. S. Xie and Y. C. Zeng, *Ind. Eng. Chem. Res.*, **51**, 5346 (2012).
15. S. Xie, W. L. Han, G. J. Jiang, and C. Chen, *J. Mater. Sci.*, **53**, 6991 (2018).
16. J. J. Jia, S. Xie, and C. D. Zhang, *ACS Omega*, **6**, 30012 (2021).
17. Y. Yang and Y. C. Zeng, *Ind. Eng. Chem. Res.*, **59**, 10664 (2020).
18. Y. D. Wang, C. C. Ji, and J. P. Zhou, *e-Polymers*, **19**, 612 (2019).
19. C. C. Ji and Y. D. Wang, *e-Polymers*, **20**, 724 (2020).
20. H. M. Krutka and R. L. Shambaugh, *Ind. Eng. Chem. Res.*, **41**, 5125 (2002).
21. H. M. Krutka, R. L. Shambaugh, and D. V. Papavassiliou, *Ind. Eng. Chem. Res.*, **42**, 5541(2003).
22. H. M. Krutka, R. L. Shambaugh, and D. V. Papavassiliou, *Ind. Eng. Chem. Res.*, **43**, 4199 (2004).
23. Y. F. Sun and X. H. Wang, *J. Text. Inst.*, **102**, 65 (2011).
24. Y. F. Sun and X. H. Wang, *J. Appl. Polym. Sci.*, **115**, 1540 (2010).
25. X. B. Hao and Y. C. Zeng, *Text. Res. J.*, **89**, 3221 (2019).
26. C. C. Ji, Y. D. Wang, and Y. F. Sun, *J. Ind. Text.*, **50**, 1409 (2021).
27. Y. D. Wang, J. P. Zhou, and X. P. Gao, *ACS Omega*, **5**, 13409 (2020).
28. Y. D. Wang, Y. P. Qiu, C. C. Ji, X. H. Wang, and F. W. Guan, *Text. Res. J.*, **92**, 423 (2022).
29. Y. D. Wang and X. H. Wang, *Polym. Eng. Sci.*, **54**, 110 (2014).
30. C. C. Ji, K. Y. Zhang, Y. D. Wang, and X. H. Wang, *J. Text. Res.*, **40**, 175 (2019).
31. F. R. Menter, *AIAA J.*, **32**, 1598 (1994).
32. M. A. J. Uyttendaele and R. L. Shambaugh, *AIChE J.*, **36**, 175 (1990).
33. B. R. Shambaugh, D. V. Papavassiliou, and R. L. Shambaugh, *Ind. Eng. Chem. Res.*, **50**, 12233 (2011).
34. V. Bansal and R. L. Shambaugh, *Ind. Eng. Chem. Res.*, **37**, 1799 (1998).
35. N. Hoda, F. Mert, F. Kara, H. G. Atasagun, and G. S. Bhat, *Fiber. Polym.*, **22**, 285 (2021).